Northumbria Research Link

Northumbria University
NEWCASTLE

University Library

Key Points:
- Space-based observations suggest onset processes are linked to a broadband ULF wave source near 10 R_E
- Longer period waves are seen first and spread fastest in the ionosphere; shorter periods spread more slowly and are more confined
- Communication to the ground is period dependent, likely resulting from preferential damping of shorter periods

Correspondence to:
A. W. Smith,
andy.w.smith@ucl.ac.uk

Diagnosing the Time-Dependent Nature of Magnetosphere-Ionosphere Coupling via ULF Waves at Substorm Onset

A. W. Smith[1] [iD], I. J. Rae[1,2] [iD], C. Forsyth[1] [iD], C. E. J. Watt[2,3] [iD], K. R. Murphy[4] [iD], and I. R. Mann[5] [iD]

[1]Mullard Space Science Laboratory, University College London, Dorking, UK, [2]Department of Mathematics, Physics and Electrical Engineering, Northumbria University, Newcastle upon Tyne, UK, [3]Department of Meteorology, University of Reading, Reading, UK, [4]Department of Astronomy, University of Maryland, College Park, MD, USA, [5]Department of Physics, University of Alberta, Edmonton, Alberta, Canada

Abstract Azimuthal structuring is usually observed within the brightening auroral substorm onset arc; such structure has been linked to the exponential growth of electromagnetic ultralow-frequency (ULF) waves. We present a case study investigating the timing and frequency dependence of such ULF waves on the ground and in the near-Earth magnetotail. In the magnetotail, we observe an increase in broadband wave power across the 10- to 100-s period range. On the ground, the arrival times spread from an epicenter. The onset of longer period waves occurs first and propagates fastest in latitude and longitude, while shorter periods appear to be more confined to the onset arc. The travel time from the spacecraft to the ground is inferred to be approximately 1–2 min for ULF wave periods between 15 and 60 s, with transit times of 60 s or less for longer period waves. This difference might be attributed to preferential damping of the shorter period waves, as their amplitude would take longer to rise above background levels. These results have important consequences for constraining the physics of substorm onset processes in the near-Earth magnetotail and their communication to the ground.

Plain Language Summary Bead-like structures are often observed within the brightening aurora that denotes the start of the explosive auroral substorm. These beads have been linked to magnetic field fluctuations, whose origin is in near-Earth space. We have studied these fluctuations using an array of magnetometers across the North American continent, as well as several spacecraft. The spacecraft observations have been used to characterize the fluctuations at their source in near-Earth space and rule out several physical mechanisms that could cause these fluctuations. On the ground, we find that the longest period fluctuations spread the fastest. Meanwhile, shorter period fluctuations are observed in a more limited region near the brightening aurora. We also investigate the travel time for the disturbances to go from space to the ground, finding it takes ∼1–2 min for the information of magnetic fluctuations to be communicated from near-Earth space to the ground.

1. Introduction

Magnetospheric substorms are typically described by a series of three phases: the growth, expansion, and recovery phases (Akasofu, 1964; McPherron, 1970). During the growth phase, magnetospheric flux is opened through dayside reconnection with the interplanetary magnetic field (IMF) carried by the solar wind. The open flux convects through the magnetotail lobes and is stored on the nightside of the Earth. This open magnetospheric flux is closed by reconnection in the magnetotail current sheet in the expansion phase (Hones, 1976).

During the expansion phase, a series of phenomenon occur in the near- and mid-magnetotail within an interval of a few minutes (e.g., Baker et al., 1996; Lui, 1996; Ohtani, 2004). In the mid-tail (∼200–25 R_E downtail), magnetic reconnection occurs which generates strong Earthward flows (Hones et al., 1984), known as bursty bulk flows (BBFs) (Angelopoulos et al., 1992; Baumjohann et al., 1990), as well as complex magnetic structures (e.g., Imber et al., 2011; Slavin et al., 1989, 1995). Meanwhile, closer to Earth (∼10 R_E downtail), the cross-tail current is diverted into the ionosphere, forming the substorm current wedge (SCW) (Atkinson, 1967; Kepko et al., 2015; McPherron et al., 1973). Two popular paradigms explaining the

sequence of these processes are the "outside-in" and "inside-out" models, although others have been proposed in more recent years (e.g., Nishimura et al., 2010). In the near-Earth neutral line (NENL) model ("outside-in"), magnetic reconnection in the mid-tail initiates the expansion phase (Baker et al., 1996). The subsequent earthward flows slow as they approach the dipolar field lines closer to Earth, disrupting the cross-tail current system and forming the SCW (Nagai et al., 1997; Shiokawa et al., 1997, 1998). Alternatively, in the current disruption (CD) model ("inside-out") a plasma instability near the inner edge of the plasma sheet leads to a divergence of the cross-tail current, the SCW (Lui, 1996). Then, rarefaction waves propagate downtail to trigger reconnection in the mid-tail (Lui et al., 1991; Roux et al., 1991). Several case studies have been presented that favor the outside-in NENL model (Angelopoulos et al., 2008; Kepko et al., 2009), the inside-out CD model (Rae, Mann, Angelopoulos, et al., 2009), or the possibility of both paradigms operating independently (Murphy et al., 2014). The precise sequence of events is unclear to this day, with the large spatial volume and relative sparsity of data coverage in the magnetotail preventing clarity.

In the ionosphere, the start of the expansion phase is traditionally identified from a rapidly brightening auroral arc (Akasofu, 1977). The brightening arc is temporally coincident with the strong growth of ultralow-frequency (ULF) wave power on the ground. These ULF waves are mostly associated with the Pi1 and Pi2 bands, with periods of 1–40 and 40–150 s, respectively (Jacobs et al., 1964). Pi2 waves have traditionally been associated with the initial magnetospheric disturbance at expansion phase onset, as well as the establishment of the SCW (Atkinson, 1967; Lester et al., 1983; Olson, 1999). After substorm onset, Pi2s have also been inferred to be a result of flows (Kepko & Kivelson, 1999; Murphy, Rae, Mann, Walsh, et al., 2011), caused by magnetic reconnection in the mid-tail (Keiling et al., 2006). Meanwhile, Pi1 band waves have been observed in a more localized region close to onset and have been related to filamentary current structures (Arnoldy et al., 1987; Bosinger & Yahnin, 1987; Wing et al., 2013). Previous studies have shown that while any given event may have a dominant frequency, there is no evidence that a single dominant frequency exists from event to event. The frequency changes, and thus statistically, the power spectra are a power law (Murphy, Rae, Mann, & Milling, 2011). With this in mind, recent work that has focused specifically on substorm onset has often used a combination of the two period bands, denoted Pi1–2 and spanning the approximate period range 24–96 s (Milling et al., 2008; Murphy et al., 2009; Murphy, Rae, Mann, & Milling, 2011; Rae et al., 2011). Recently, Rae et al. (2017) investigated the relative timing of Pi1, Pi1–2, and Pi2 band waves, finding that Pi1–2s are the first to arrive at the ground followed by Pi2s. Lastly, the shorter period Pi1s arrive.

Nosé et al. (1998) first developed an algorithm to recognize substorm onset by identifying when Pi2 pulsations rose above background levels, using wavelet-based analysis methods. This work was later extended by Milling et al. (2008), who found that ULF waves with periods of tens of seconds were first to rise above a noise threshold; i.e., Pi1–2 waves. Additionally, when applied to a wide array of magnetometers, the onset of Pi1–2 waves was found to spread from a coherent epicenter, which defined the location where the SCW subsequently formed. Murphy et al. (2009) have since shown that this epicenter is co-located with the location at which the first global auroral intensification occurs and also that the ULF wave onset precedes global auroral breakup by several minutes.

The onset location and epicenter of Pi1–2 ULF waves have been found to be spatially and temporally coincident with azimuthal structures that develop in the brightening auroral arc (Rae, Mann, Angelopoulos, et al., 2009; Rae & Watt, 2016; Rae, Mann, Murphy, et al., 2009; Rae et al., 2017), often termed auroral beads (Henderson, 1994). Similar auroral beads have been observed in conjugate hemispheres (Motoba et al., 2012), suggesting that they share a magnetospheric source. Mapping auroral beads into the magnetotail suggests that they originate between 8–12 R_E downtail (Donovan et al., 2008; Kalmoni et al., 2015, 2018). Numerous studies have shown ULF wave activity in this region close to the time of substorm onset (e.g., Chang & Cheng, 2015; Chaston et al., 2012; Ergun et al., 2015; Keiling, 2012; Lui et al., 2008; Motoba et al., 2015; Panov et al., 2012; Saito et al., 2008; Uritsky et al., 2009; Uozumi et al., 2020; Walsh et al., 2010). Most recently, Smith et al. (2020) showed excellent statistical correspondence between ground- and space-based observations of increasing Pi1–2 wave power around substorm onset, demonstrating that there is a consistent source region in the magnetotail.

Despite these earlier works, there remain significant uncertainties about the sequence of events surrounding magnetospheric substorm onset. In this study, we analyze the relative timing and period dependence of

Pi1–2 (10–100 s) waves prior to substorm onset using a large array of ground magnetometers and space-based observations. We compare and contrast the space- and ground-based observations and calculate the expected travel time of the disturbances from the magnetotail to the ground. Our results reveal not only how ULF waves can be used to probe onset processes, but that the combination of continent-scale ground magnetometer coverage with multisatellite in situ measurements reveals details of the magnetospheric source and nature of magnetosphere-ionosphere coupling.

2. Data and Method

This study uses a combination of data from ground- and space-based observatories. In space, we use data from the Time History of Events and Macroscale Interactions during Substorms (THEMIS) mission (Angelopoulos, 2008). Three spacecraft (the A, D, and E THEMIS probes) provided passes through the near-Earth plasma sheet in early 2009. During the interval of study here, the spacecraft also mapped to the North American continent, a region covered with a dense network of ground magnetic observatories. From the spacecraft, we use data from the onboard magnetometers (Auster et al., 2009), supplemented with data from the electrostatic analyzers (McFadden et al., 2009). On the ground, we use data provided by the Canadian Array for Realtime Investigations of Magnetic Activity (CARISMA) (Mann et al., 2008), THEMIS (Russell et al., 2008), Canadian Magnetic Observatory System (CANMOS), Geophysical Institute Magnetometer Array (GIMA), and Midcontinent Magnetoseismic Chain (McMAC) magnetometer arrays.

In this study, we utilize the horizontal component of the ground magnetic field by combining the north-south and east-west components by summation in quadrature. For the space-based data, the perpendicular components are calculated from a mean field aligned (MFA) coordinate system, with a window of 200 s used to calculate the background field orientation. The perpendicular components are then combined by summation in quadrature. We have selected the horizontal ground and perpendicular space components as they should be directly comparable between the ground and space, as both are perpendicular to the background field. This choice also means that our results are directly comparable to previous works on this topic (e.g., Milling et al., 2008; Murphy et al., 2009), which did not want to make assumptions as to the polarization of the waves (c.f., Lester et al., 1983). Meanwhile, the 200-s window was selected so as to be twice the length of the maximum period wave of interest (i.e., twice 100 s). The horizontal/perpendicular field is then broadly bandpass filtered between 5 and 200 s to isolate the periods of interest (i.e., the Pi1–2 regime).

In contrast to the orthogonal Meyer wavelet (Meyer, 1990) and discrete wavelet transform (DWT) employed by Nosé et al. (1998), Milling et al. (2008), and Murphy et al. (2009), we use a nonorthogonal Morlet wavelet (Morlet et al., 1982) and continuous wavelet transform (CWT) to quantify ULF wave power at substorm onset as a function of time and wave period. The use of a nonorthogonal wavelet and CWT means that we are not restricted as to the scales (effectively periods) we can test (Farge, 1992), therefore effectively allowing us a higher resolution (depending on the selected wavelet). The use of a wavelet transform removes the necessity to select time windows, such as would be required for a similar windowed Fourier analysis (e.g., Kaiser & Hudgins, 1995), and allows consistent analysis over different period bands. For full details of the CWT method employed, the interested reader is directed to Torrence et al. (1998).

The Morlet wavelet has been selected as to provide a good balance between frequency and time resolution. Wavelets with higher time resolution were found to greatly, and undesirably, broaden the wavelet period uncertainty (e.g., the Paul wavelet; Torrence et al., 1998), negating the benefit of the CWT. In this study, the calculated wavelet power spectra have also been rectified to account for a scale-dependent factor, as suggested by Liu et al. (2007). Finally, we evaluate the statistical significance of the signals in the power spectrum by comparing them to a univariate lag-1 autoregressive noise model (c.f., Torrence et al., 1998). This noise model is defined using an interval of data obtained 90 min prior to substorm onset. Following the work of Murphy et al. (2009), we define the point at which each period band rises above the 2σ significance level to be the onset of ULF activity, meaning that the signal is significant at the 95% level.

3. Results

We present a case study from the onset of a substorm that started at 06:06 UT on 23 March 2009. The substorm was identified using the Substorm Onsets and Phases from Indices of the Electrojet (SOPHIE) technique (Forsyth et al., 2015). The SOPHIE method identifies the start of the expansion phase by selecting when
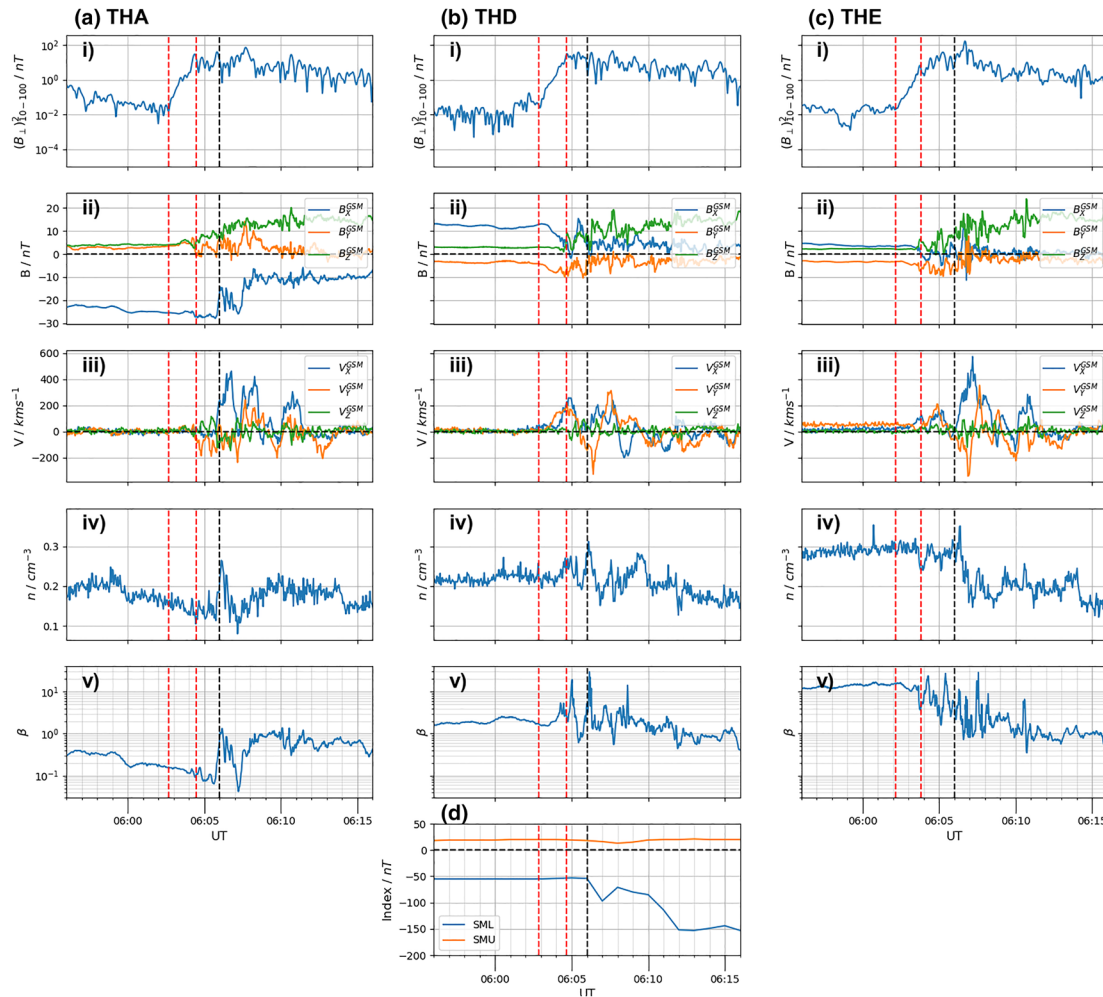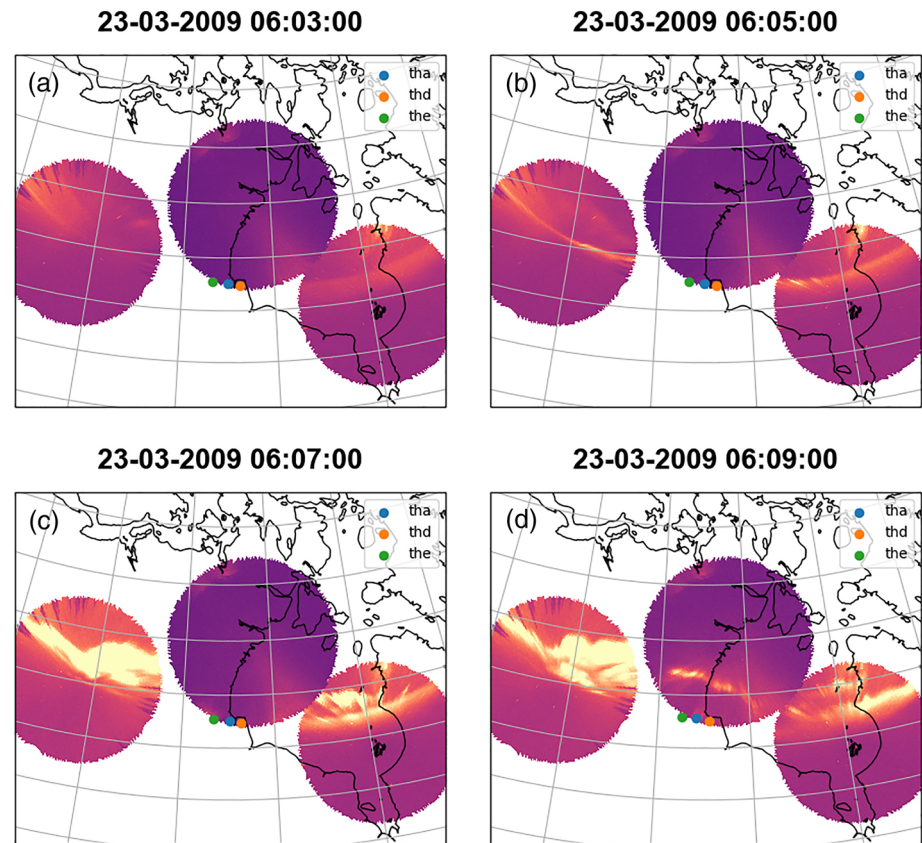
Figure 1. THEMIS A, D, and E observations for a 20-min interval around substorm onset on 23 March 2009 at 06:06 UT. The three columns (a, b, and c) represent the observations of each of the three spacecraft (A, D, and E). The rows display: (i) the perpendicular wave power between 10 and 100 s, (ii) the magnetic field in GSM coordinates, (iii) the ion velocity in GSM coordinates, (iv) the ion density, and (v) the ion β. The black vertical dashed line indicates the substorm onset as identified from the rate of change of the SML index (Forsyth et al., 2015); the SML and SMU indices are shown in Panel d. The vertical red dashed lines indicate the approximate start and end of the exponential increases in perpendicular wave power between 10 and 100 s.

the auroral SML index begins decreasing at a significant rate. This time therefore corresponds to the formation of the large scale SCW. This substorm was selected as it presents as an isolated onset, with no other significant substorm activity within the preceding 90 min. Meanwhile, as will be shown, all three THEMIS spacecraft were located close to the onset location.

3.1. Space and Ground Observations

Figure 1 shows THEMIS A, D, and E spacecraft observations (Figures 1a–1c, respectively) for a 20-min interval centered on the SOPHIE defined substorm onset at 06:06 UT, which itself is indicated with a vertical dashed black line. From Figure 1d, showing the SML and SMU indices recorded during this interval, the SOPHIE method can be seen to have identified the start of a substantial decrease in SML, signifying the formation of the SCW. Prior to 06:02 UT, all three spacecraft saw little variability in the magnetic field or ion velocities (Figure 1, ii and iii), confirming that the interval was relatively quiet prior to onset. THEMIS A was located near the edge of the plasma sheet, as indicated by $|B_X| \sim 20$ nT, an ion density of ~ 0.2 cm^{-3} and a plasma beta of ~ 0.2 (Figure 1a). Meanwhile, THEMIS D and E were located within the plasma sheet, with $B_X \leq 15$ nT, ion densities exceeding 0.2 cm^{-3}, and with values of the plasma β greater than 1 (Figures 1b and 1c) (e.g., Angelopoulos et al., 1994; Sergeev et al., 2015).

23-03-2009 06:03:00   **23-03-2009 06:05:00**

**23-03-2009 06:07:00**   **23-03-2009 06:09:00**

Figure 2. Combined THEMIS ASI observations from the FSMI, RANK, and SNKQ ground stations for (a–d) four selected time intervals around the onset of the substorm on 23 March 2009 at 06:06 UT. The three THEMIS spacecraft (A, D, and E) are mapped to the ground using the model of Tsyganenko and Sitnov (2005) and are included as colored circles.

Just after 06:02 UT, all three spacecraft observed clear increases in the 10- to 100-s filtered perpendicular wave power of over three orders of magnitude, outlined with red dashed lines (Figures 1a–1c, i). The elevated wave power at all three spacecraft persists through the SOPHIE-defined substorm onset which occurs ~70–120 s after the wave power is fully developed. Following SOPHIE onset, THEMIS A and E observe strong earthward flows of at least 400 km(Figures 1a and 1b, iii), likely BBFs related to reconnection occurring tailward of the spacecraft.

Moving to the ground, Figure 2 shows optical observations of the aurora at 2-min intervals around substorm onset. The mapped locations of the THEMIS spacecraft have been calculated using the model of Tsyganenko and Sitnov (2005). Between 06:03 and 06:05 (Figures 2a and 2b), the aurora can be seen to brighten significantly either sides of the mapped spacecraft locations. Azimuthal structure characteristic of auroral beads is also apparent in the brightening arc, particularly east of the mapped spacecraft locations. Following onset, the arc can be seen to brighten significantly and move poleward (Figures 2c and 2d). Figure 2 provides strong evidence that the THEMIS spacecraft may be located close to phenomena associated with auroral beads. The GILL ground station, almost co-located with the mapped spacecraft locations and likely auroral onset, has not been included in Figure 2 as it is unfortunately contaminated by cloud cover in this interval. This has the unfortunate effect that more quantitative analysis of the azimuthal auroral structure is not possible for this event (c.f., Kalmoni et al., 2015, 2017).

Figure 3 further investigates the growth in space-based wave power, once more presenting the 20-min interval around SOPHIE-defined onset. Figure 3a shows the increase in 10- to 100-s filtered perpendicular wave power, previously highlighted in Figure 1. During this interval, the THEMIS spacecraft were all located pre-midnight and around 11 R_E downtail (Figures 3e and 3f). Notably, THEMIS D is longitudinally offset from the other two spacecraft, perhaps explaining the lack of strong earthward flows that were observed by THEMIS A and E in Figure 1.
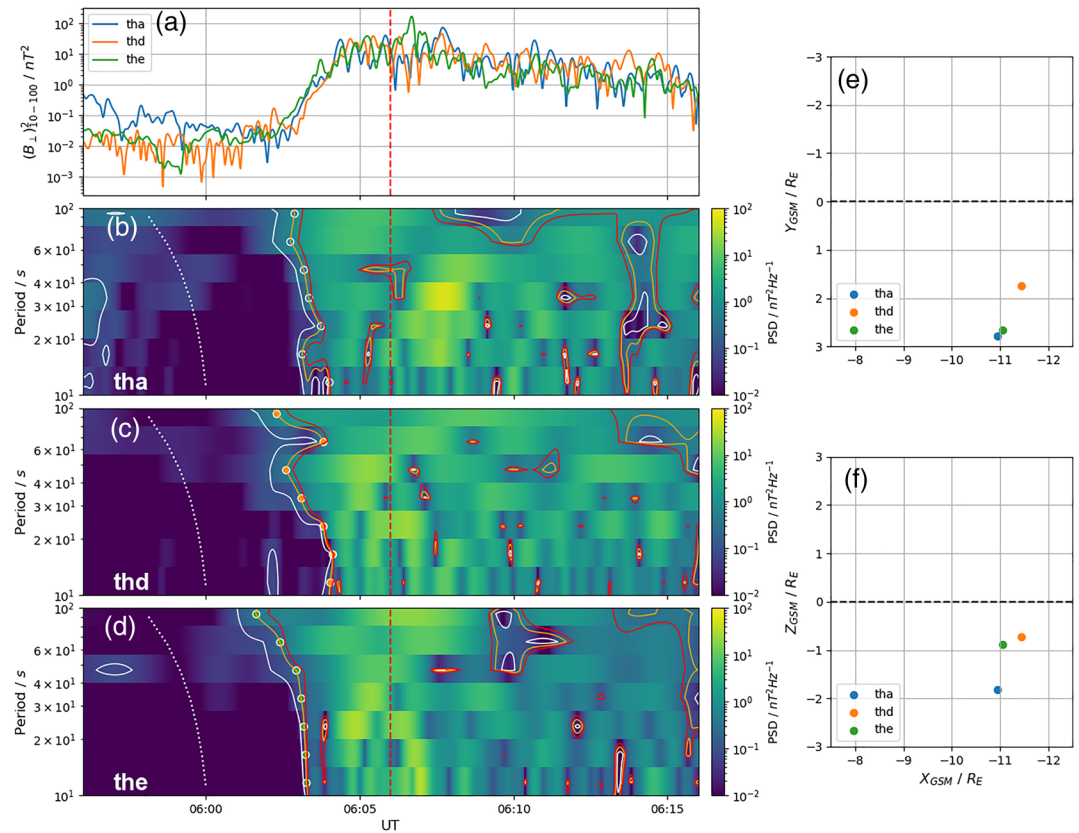
Figure 3. THEMIS A, D, and E observations for a 20-min interval around substorm onset on 23 March 2009 at 06:06 UT. The figure presents the following: (a) the filtered perpendicular wave power in MFA coordinates between 10 and 100 s, (b–d) the CWTs of the perpendicular field for THEMIS A, D, and E, and (e and f) the locations of the spacecraft in the *X-Y* and *X-Z* plane. The white, orange, and red solid lines indicate the 1, 2, and 3σ significance contours, respectively. The dotted white line at around 06:00 on the CWTs (b–d) represents the increasing uncertainty in the wavelet timing with increasing period, plotted for a signal of each period at 06:00. The white outlined circles highlight the 2σ significance contour, showing the time at which each period band rose above 2σ. The red vertical dashed line indicates the substorm onset as identified from the rate of change of the SML index (Forsyth et al., 2015).

Figures 3b–3d show CWTs of the perpendicular magnetic field at each of the spacecraft, with the color bar showing wave power as a function of period and time. Around 06:00 UT, wave power in all bands and at all spacecraft is below $\sim 10^{-2}\,\mathrm{nT^2\,Hz^{-1}}$, as indicated by the blue shading. Following this, the exponential increase in wave power just prior to 06:05 UT can be seen in the spectrograms, with all period bands rapidly rising several orders of magnitude through the significance levels to $\sim 10^{-1}$ to $10^{-2}\,\mathrm{nT^2\,Hz^{-1}}$. The spectrograms also show that long period wave power appears to increase first. However, we know that the timing uncertainty of the longer period bands is greater than the shorter period bands. To address this concern and determine if the result is purely caused by the wavelet method, we can analytically calculate the timing uncertainty expected at each period as a result of the Morlet wavelet. The relative uncertainty is plotted (subtracted from 06:00 UT) as a white dotted line in Figures 4b–4d. The inference being that if the rise in wave power (or significance contour) follows a trend parallel to the dotted line, then it would be consistent with a simultaneous increase in wave power in all bands, and the difference in timing between the long and short periods would be attributable to the method and not the observations themselves. In general, we see that in Figures 4b–4d, the difference in the timings of the wave bands exceeding the 2σ level closely follows this line, therefore suggesting that the true timings of the increase in power were very similar.

Figure 4 shows the response of six ground stations during the same interval. Figure 4a shows a map of North America, on which the ground stations used in the study are plotted as black crosses or colored squares. Figures 4b–4g show CWTs for the six ground stations indicated with colored squares in Figure 4a. These stations have been selected as examples that are either close to the mapped locations of the spacecraft, at a
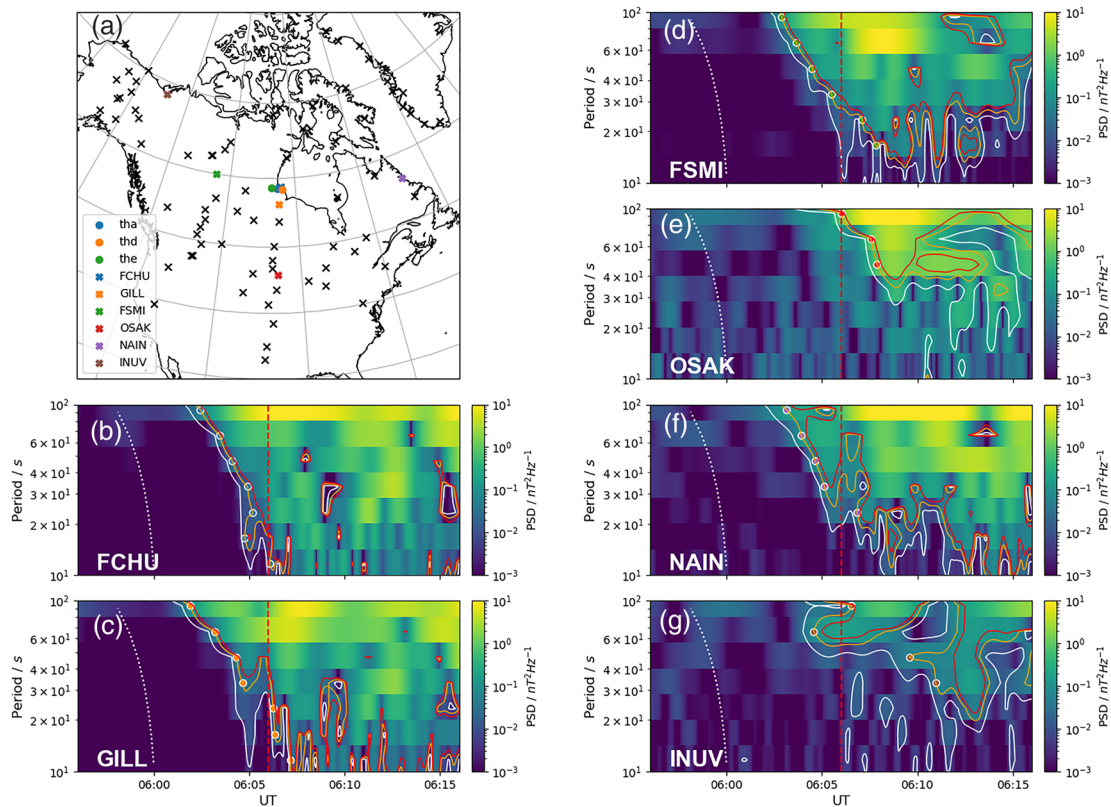
Figure 4. Magnetic ground station observations for a 20-min interval around substorm onset at 06:06 UT on 23 March 2009, presented on a geographical grid. (a) A map of the ground stations included in the study is provided, where the stations are indicated with crosses, while (b–g) CWTs for a subset of the stations (indicated on the map with colored crosses) are also shown. The complete set of ground stations included in this study are indicated in black. The mapped locations of the THEMIS spacecraft are presented with colored circles. The CWTs (b–g) are presented as in Figure 3.

lower latitude, or are displaced in longitude along the auroral zone. The mapped locations of the THEMIS spacecraft, calculated using the model of Tsyganenko and Sitnov (2005), are included as colored circles.

The stations close to the mapped spacecraft locations, in Figures 4b and 4c (FCHU and GILL, respectively), show similar signatures to the spacecraft in Figure 3, though the shortest periods appear to show weaker power and are slightly delayed. This is also the case for the station to the west of the spacecraft, in Figure 4d (FSMI), where the lower periods are clearly more delayed, rising above 2σ after the SOPHIE onset. Additionally, at FSMI, significant wave activity does not appear to be present in the lowest period band shown. Similar observations are made at NAIN to the east (Figure 4f). Meanwhile, the station located at lower latitudes (OSAK), in Figure 4e, does not show ULF wave activity above 2σ significance below a period of ~40 s. Likewise, the westernmost station (INUV), in Figure 4g, shows a weaker but significant ULF wave signature that is truncated at low periods.

These stations highlight the variable timing at which observations of ULF wave power exceed the 2σ significance level. Additionally, not all stations observe significant wave power at all periods, and we therefore now investigate the spread and timing of wave power in different period bands using the full array of magnetometer stations.

3.2. Period-Dependent Onset Maps

Combining the information from all of the stations shown in Figure 4a allows maps to be created showing the relative timing of ULF wave onset as a function of wave period. At each station, the onset time of ULF wave activity in each of the spectrogram period bands is taken as the time at which the wavelet power exceeds 2σ of the background (e.g., Murphy et al., 2009). Figure 5 shows maps of the relative delays of each period band, with white contours placed every 60 s. This spacing has been chosen to approximately correspond to the timing uncertainty of the Morlet wavelet for the longest period (63-s uncertainty in the 93.5-s
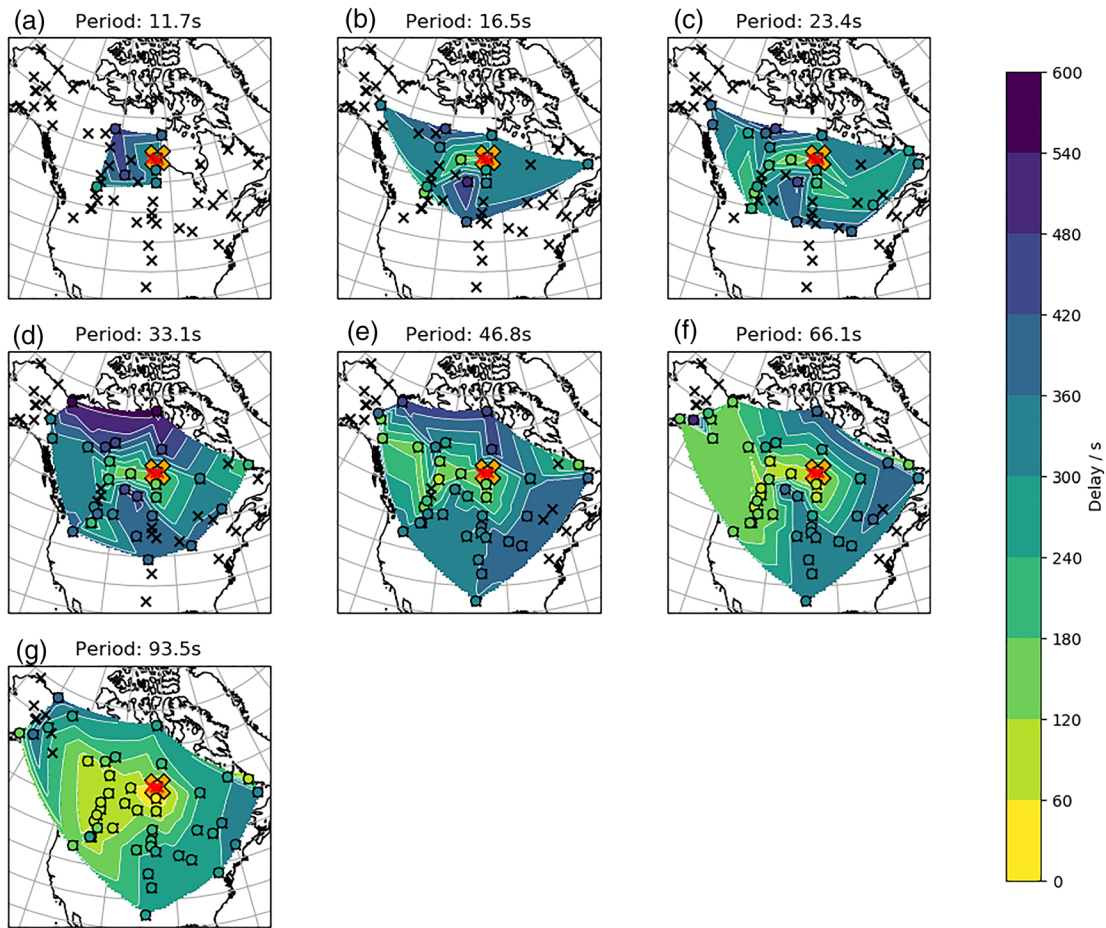
Figure 5. Maps showing the relative delays at which each ground station observed ULF wave activity above 2σ of background. The delay is calculated relative to the first observation of significant ULF activity, at any station or period: for this event this is the GILL station at 06:01:54 in the 93.5-s period band. Each panel shows a period band, with the period increasing in subsequent panels. Stations for which no elevated ULF wave activity were observed in that period band are indicated with black crosses, while the color of the other stations denotes the relative delay of ULF onset. A 2D linear interpolation of the stations is shown in the background, discretized at 60-s intervals. The footprints of the THEMIS spacecraft, mapped with the model of Tsyganenko and Sitnov (2005), are indicated with red crosses. The gold cross in each panel indicates the location of substorm onset, as determined by the SOPHIE technique (Forsyth et al., 2015).

band) and is consistent between panels. The delays are calculated relative to the first time any band at any station exceeded 2σ of the background. For this event, the GILL station, located a few degrees south of the mapped spacecraft, was the first to see significant ($\geq 2\sigma$) ULF wave activity at 06:01:54 UT in the 93.5-s band. The maps are created using a 2D linear interpolation scheme from the sparse ground station data. Specifically, the griddata function from the Python Scipy interpolate module has been used.

Most notably from Figure 5, a clear epicenter is observed at almost all ULF wave periods presented; this epicenter is approximately co-located in all bands and is slightly equatorward and westward of the mapped spacecraft locations. The substorm onset location determined through the SOPHIE technique is located marginally eastward and northward of this ULF wave epicenter. Significant ULF wave activity at lower periods (e.g., 11.7 and 16.5, Figures 5a and 5b) appears to be much more localized than at longer periods. The longer ULF periods (66.1 and 93.5 s, Figures 5f and 5g) can be seen to be the first to rise above the background at more stations, i.e., with the smallest relative delay. It is also apparent that the contours are more broadly spread at the longest periods, with the spatial gradient of the delay increasing as the period decreases. This suggests that the ULF wave onset spreads fastest at the longer periods. The onset times also appear westward of the onset with the shortest relative delay, for periods greater than ~30 s.

Interestingly, for longer periods (e.g., $\gtrsim 40$ s), it is possible that a second epicenter is also observed, at a lower latitude and displaced westwards of the main epicenter. This is clearest in Figure 5f, where a
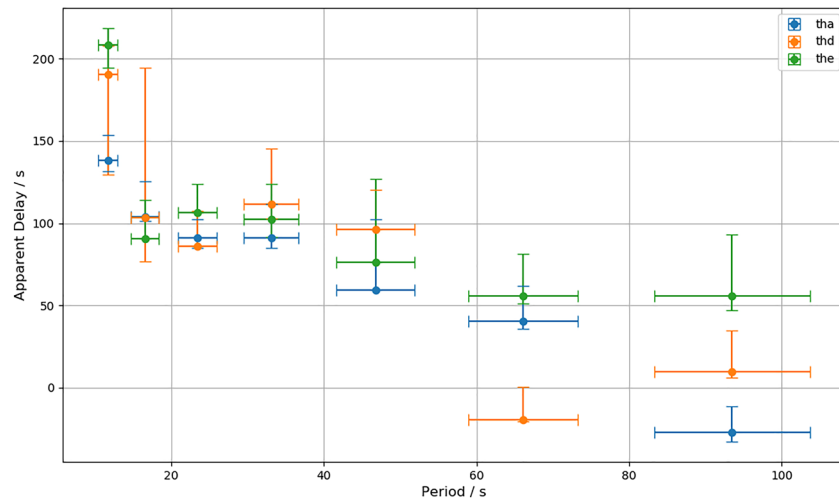
Figure 6. The space-ground time delay between the THEMIS spacecraft observing ULF waves 2σ over background, and the time at which the mapped spacecraft location (interpolated from the maps in Figure 5) would observe the onset of ULF wave activity, plotted as a function of period. The uncertainty in the relative delays are calculated as the maximum and minimum observed when the spacecraft mapping is varied by ±1° of latitude and longitude. The uncertainty in the period is provided by the use of the Morlet wavelet.

cluster of stations south and west of the main epicenter show relatively short delays and are separated from the main epicenter by stations that observe very long delays (600 s or greater). The second epicenter is not clearly seen in the longest period (93.5 s), perhaps as they both merge into a single large epicenter when the contours are set to 60 s. It is noteworthy however that ground based magnetometers will average their response over a large spatial region, and so there is an additional source of uncertainty which may broaden any signature.

3.3. Magnetosphere-Ionosphere Travel Times

Assuming that the disturbance originates in space, the difference in timing between the measurements made in space (Figures 3b–3d) and those seen on the ground (Figure 5) corresponds to an effective travel time from the near-Earth magnetotail to the ground. We can extract the expected timing of the arrival of the signals on the ground at the magnetically conjugate location of the spacecraft from the interpolated map in Figure 5 and compare it to the observed wave onsets in situ in the magnetotail in Figure 3. The results of this process are plotted in Figure 6. During the disturbed interval of substorm onset, the spacecraft mapping may have a considerable spatial uncertainty, and so we calculate a timing uncertainty by varying the spacecraft mapping. If we adjust the solar wind input of the magnetospheric model by ±15 min, we return approximately a 1° variation in spacecraft footprint, predominantly in the longitudinal direction. We therefore vary the mapped spacecraft location by ±1° and present the maximum and minimum delays returned as the error bars. Meanwhile, the uncertainty in the period is calculated analytically from the Morlet wavelet.

Between periods of ~15 and 30 s, the delay to the ground can be seen to be ~90–120 s. Above this period, the delays appear to be shorter, of the order of ~60 s. At the two longest periods, THA (THEMIS A) and D show very low delays. In contrast, THE shows a delay of ~60 s, more consistent with the lower periods. Empirically, the reason for the discrepancy between the results from THA and D and those from THE can be seen in Figures 3b and 3c, where the morphology of the CWTs does not follow the same pattern as THE in Figure 3d. The CWT from THE can be seen to strongly mimic the wavelet uncertainty curve on the left, suggesting a single onset time for all periods. When slices of the wavelet spectrograms are inspected, we find that the exponential increases of the PSD of the longest period bands for THA and THD are not as clear as for THE. It could be that THA and THD are further from the onset epicenter, as evidenced by their later observations, and therefore, there may be some difference in travel path or mode coupling of the longer period waves.

4. Discussion

We have presented a case study comparing the timing and period dependence of ULF wave onset in the Pi1-2 band, on the ground and in the near-Earth magnetotail. ULF waves in the 10- to 100-s period range on the ground have previously been linked to azimuthal auroral structures (Rae et al., 2010) and associated with magnetotail processes occurring at substorm expansion phase onset (Rae, Mann, Murphy, et al., 2009; Rae, Mann, Angelopoulos, et al., 2009; Walsh et al., 2010). In contrast to previous studies, we employ a CWT technique which provides a smaller uncertainty in period thereby providing better period resolution and hence temporal resolution as well. By using this technique, we can also infer a period-dependent travel time between space- and ground-based observations.

4.1. Near-Earth Magnetotail Comparison

Comparing Figures 3 and 4, some similarities and differences are apparent in the wavelet power spectra measured on the ground and in space. In space (Figure 3), the wavelet spectrograms exceed 2σ of the background ~5 min earlier than the formation of the large-scale SCW, whose DC magnetic field change is determined by the SOPHIE method. Additionally, from the space-based observations in Figure 1, the wave power grows several minutes prior to the arrival of BBFs at the spacecraft, suggesting that the waves are generated by a distinct phenomenon. The relative timings in space are mostly consistent with a broadband source, especially when accounting for the timing uncertainty of the wavelet technique. It can also be seen that the observations at THEMIS E precede those of the other two spacecraft, which are vertically (THA) and azimuthally displaced (eastward, THD). This indicates that, for this event, THE is located closer to the source of ULF wave power in the tail.

Previously, ground observations of ULF waves in the period range investigated here have been observed to grow exponentially prior to substorm onset (Rae et al., 2011). Similarly, co-located exponential growth has been found in the auroral brightness as well as the growth of low azimuthal wave number structures in the brightening arc (Kalmoni et al., 2015, 2017; Rae et al., 2010, 2012). Meanwhile, self-similar conjugate auroral structures are observed in both hemispheres (e.g., Motoba et al., 2012). Together, these observations have been used to suggest that the mechanism of auroral beading and ULF waves at substorm expansion phase onset is in the magnetotail. The results here confirm that the ULF wave power is first observed in the magnetotail and then subsequently in the ionosphere (e.g., Smith et al., 2020). Additionally, we have presented ground ASI images showing the conjugate development of auroral beads in the brightening arc. Previous studies have used the exponential growth in ULF wave power to infer that the linear stage of a magnetospheric instability is active shortly prior to onset (c.f., Lui, 2004). Candidate instabilities include the cross-field current instability (Lui et al., 1991), shear flow (e.g., Voronkov et al., 1997) and kinetic ballooning instabilities (e.g., Cheng, 2004), and the current-driven Alfvénic instability (Perraut et al., 2000). Our observation that the in situ ULF waves are broadband suggests that narrowband instabilities, such as the current-driven Alfvénic instability, can likely be ruled out for this event. However, it is possible that the picture is more complex with multiple relevant processes occurring; for example, a narrowband instability may be exciting a broadband response in a larger spatial region. Nevertheless, these observations place direct constraints on the instability and its coupling to the ionosphere.

As noted above, at ground stations approximately conjugate with the spacecraft (e.g., FCHU, Figure 4b), the timing of the different period bands is consistent with the space-based source. However, the wavelet spectrogram power below ~20 s is weaker than it is in space, which could be evidence of ionospheric filtering at low periods. At a moderate longitudinal separation, the FSMI station (Figure 4d) shows a much more pronounced delay at short periods, with the CWT exhibiting a strong "bend." This suggests that the short periods may take a significantly longer time to reach this station. At lower latitudes, e.g., OSAK in Figure 4e, we can see that the signal of any period below ~40 s is clearly absent. Previous studies have also noted that the short period ULF waves (e.g., $\lesssim$ 40 s) do not extend to lower latitudes (e.g., Arnoldy et al., 1987; Rae et al., 2017).

This has important implications for ULF wave substorm onset detection. Longer period ULF waves are seen over a broad region, with some delay. However, the onset region may be located much more precisely by consideration of shorter period ULF waves.

4.2. Period-Dependent Onset Maps

Using the full ground observatory arrays allowed the production of maps of the relative delay at each wavelet period. We note that there is a spatial uncertainty implicit in the use of ground magnetometer stations, whose measurements average a large region. With this in mind, the epicenters observed in Figure 5 at the different periods are consistent both with each other and with previous studies (e.g., Murphy et al., 2009; Rae, Mann, Angelopoulos, et al., 2009; Rae, Mann, Murphy, et al., 2009; Rae et al., 2010, 2011; Walsh et al., 2010). Additionally, though we have used a different convention for defining the ULF wave periods, the ~120-s lag between longer period (here ~60–90 s) and shorter period (here ~15–30 s) ULF waves is similar to that observed by Rae et al. (2017) for Pi1–2 and Pi1 waves.

We find that the onset times of waves with periods ≥60 s appear to propagate fastest in latitude and longitude: they display the broadest contours in Figure 5g. If we take the difference between the FSMI and FCHU stations (highlighted in Figure 4) we find that the onset times spread west at between 40 and 90 km, approximately 15–40 s per 10° of longitude. These onset propagation speeds are similar to those previously observed by Murphy et al. (2009) but interestingly are only found approximately westward of the onset epicenter. These speeds are much faster than the estimated expansion of the auroral westward traveling surge (WTS), which is typically less than 10 km (e.g., Roux et al., 1991). This discrepancy suggests that the ULF wave signature is not simply a manifestation of the expansion of the SCW and associated auroral bulge in the ionosphere. If we take equivalently spaced stations north, east, and south of FCHU (the RANK, SNKQ, AND PINA stations, respectively), we find the onset arrival times spread at a more moderate ~5–10 km, or several minutes per 10° of longitude/latitude. This is slower than previous estimates (e.g., Milling et al., 2008), which were themselves slower than would be estimated if modeled as spreading at the Alfvén velocity in the near-Earth magnetotail (which has been estimated to correspond to speeds of the order 5–10 s/10° of longitude; e.g., Murphy et al., 2009).

Shorter period ULF waves (e.g., 10–30 s; Figures 5a–5c) appear to be much more tightly constrained around the auroral latitudes and show much steeper latitudinal gradients in the delays, indicating the onset times at more distant stations are observed much later. Taking the same stations as tested above, we find that at shorter periods the onset spreads westward at a rate of ≤10 km, and in the other cardinal directions at a speed of ~1–5 km. Historically, Pi1s (up to 40-s periods) had been observed to be more localized to the onset region (e.g., Bosinger & Yahnin, 1987), though more recent work had since suggested that both Pi1s and Pi2s decay at the same rate and follow the same power law (Murphy, Rae, Mann, & Milling, 2011; Rae et al., 2011). Therefore, the latitudinal behavior was previously explained as Pi1s have a lower amplitude and thus reach the noise floor of the instrument faster.

The SOPHIE technique, which uses the rate of change of the SML index to identify substorms, also provides an estimate of the substorm onset location by selecting the magnetometer station from which the SML index is derived in that time interval (Forsyth et al., 2015). Around substorm onset, the SML index is expected to track the peak of the westward electrojet (Gjerloev, 2012; Newell & Gjerloev, 2011). For this substorm (Figure 5), the SML-derived onset is located on the eastward edge of the onset epicenter. Therefore, the ULF onset epicenter is likely close to the peak of the westward electrojet.

We find some evidence in this event there may be a second epicenter at relatively short delays (~60–120 s) for the longer period ULF waves, e.g., 60–90 s (Figures 5f and 5g). One epicenter is centered at auroral latitudes, slightly southwest of the mapped spacecraft, with the second at a lower subauroral latitude, to the west of the previous epicenter. It should be noted that the westward offset could be an artifact of the irregular ground magnetometer grid available. Similar observations were made by Rae et al. (2017), though without any clear azimuthal offset and discussed in terms of "Tamao travel times," i.e., time-of-flight arrival of ULF waves in the ionosphere. It has previously been suggested that there may be two distinct travel paths of Pi2 waves that minimize their time of flight (Chi et al., 2009). The first path may map to the auroral zone, while the second might be via the outer boundary of the more dense plasmasphere and consequently at lower latitudes. This may be the case for any isolated substorm onset instability in the near-Earth region, whereby a signal has sufficient time to propagate from its initiation region to the outer edge of the plasmasphere.
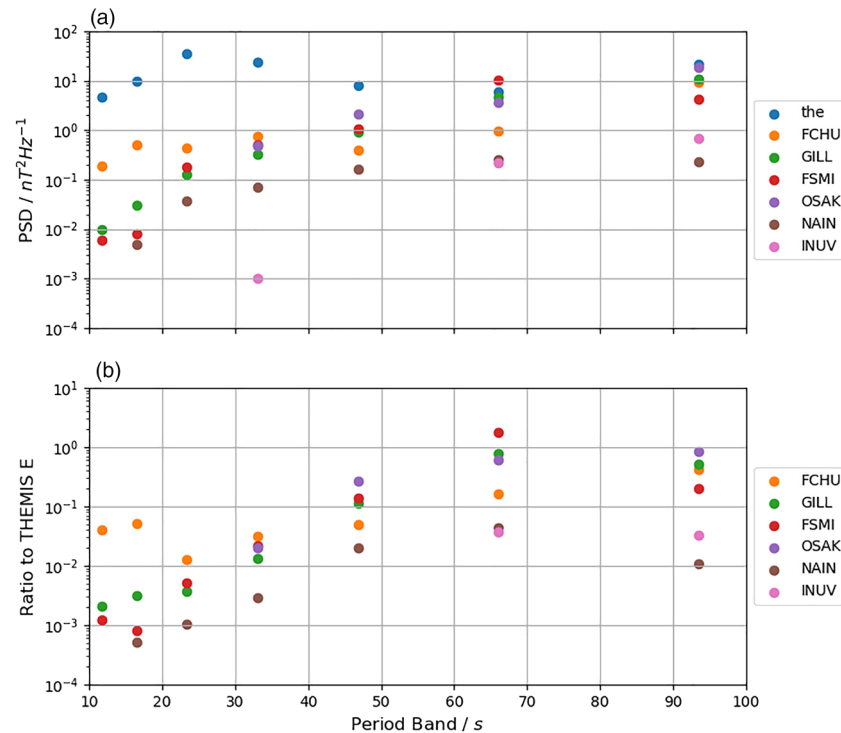
Figure 7. (a) The peak power spectral density (PSD) observed as a function wave period for the THEMIS E spacecraft and the ground stations highlighted in Figure 4. (b) The ratio of the peak PSD observed on the ground to that observed by THEMIS E.

4.3. Magnetosphere-Ionosphere Coupling Times

It is notoriously difficult to calculate accurate travel times for magneto-hydrodynamic (MHD) waves from the magnetotail to the ionosphere at substorm onset. Empirically, Smith et al. (2020) cross-correlated bandpass-filtered wavepower between 10 and 100 s, measured in space and at conjugate ground stations at substorm onset, estimating a 1- to 1.5-min delay on average.

Several studies have approached the issue of magnetosphere-ionosphere coupling through ULF waves theoretically. For example, Chi et al. (2009) used empirical models of the field (Tsyganenko, 1989), density and temperature to calculate the magnetosonic and Alfvén velocities. The travel times were calculated using the "Tamao paths" (c.f., Tamao, 1964), where initial propagation is through a fast mode wave perpendicular to the field, before the propagation couples to a parallel Alfvénic mode. Chi et al. (2009) found that the travel time from a distance of $X_{GSM} \sim -20\ R_E$ was of the order of 2–3 min. More recently, Ferdousi and Raeder (2016) tested the travel times by launching disturbances from different downtail distances in a global MHD model. It was found that the true travel paths may be more complicated than the Tamao paths, and some of the fastest modes may travel through the lobes, where the Alfvén speed is significantly higher, several thousand km. In their simulations, Ferdousi and Raeder (2016) found that the travel time for the fastest modes was estimated at ~ 70 s from approximately $-30\ R_E$.

The theoretical results discussed above are consistent with the majority of our empirical results, which find travel times between 60 and 120 s from $\sim 10\ R_E$ for Pi1–2 waves. We have also shown that the onset of different period bands are seen at different delays. This is unlikely to be an artifact of the analysis as the timing is calculated between the onsets identified in both locations with the same method, and therefore, the different timing uncertainties with wavelet period (e.g., indicated by the dotted white lines in Figures 3 and 4) are accounted for. A potential explanation could be that the phase velocity of the waves perpendicular to the field is a function of the wave period, with higher periods having a larger phase velocity. However, if shear Alfvén waves are communicating the disturbance to the ground (c.f., Kalmoni et al., 2018), then their group and phase velocity are independent of frequency. Nevertheless, the linear damping rate of such waves in

warm plasma is a function of frequency, which would act to more heavily dampen shorter period waves. If short period waves were more heavily damped then, they may appear to arrive later in the ionosphere, as their amplitudes were previously too small to be detected and would thus be below the noise threshold for longer.

To test this theory, we may evaluate the magnitude of the peak wave power in each location as a function of wave period, as is shown in Figure 7. First, we note that the peak power spectral density (PSD) observed by THEMIS E is relatively flat with period, varying by less than an order of magnitude and with no clear trend. In contrast, we see that the ground stations in Figure 7a show strongly decreasing PSD with reducing period, below ∼60 s. In Figure 7b, where we show the ratio of the peak ground station PSDs to THEMIS E, we see this trend more clearly, and an approximate exponential decrease in PSD below a period of ∼60 s at most ground stations. We note that this trend is robust to changing the comparison to THEMIS A or D; only a single comparison is presented for clarity. We would expect to see this pattern if shorter period shear Alfvén waves were damped more strongly and thus less wave power in those periods were to reach the ground. As mentioned above, this would also act to delay the apparent onset of these periods, explaining the later timing and more limited spread of the shorter periods.

It is important to note that the apparent expansion in ULF wave onsets across the magnetometer array is likely a combination of the spatial development of the magnetospheric wave source, and the propagation of the waves away from the epicenter. Disentangling these two phenomenon is challenging; however, the relative PSD peak magnitudes from ground- and space-based observations suggest that the delayed onset of short period ULF waves could be the result of damping during the propagation of the waves and not of differences in timing at the magnetospheric source itself. The fact that damping increases with frequency may suggest that the shorter period waves are associated with shorter perpendicular wavelengths and therefore experience more damping (e.g., Lysak & Lotko, 1996; Watt & Rankin, 2007).

5. Summary and Conclusions

In this paper, we have used a CWT method to compare the period content and relative timing of Pi1–2 band ULF waves at substorm onset, from space- and ground-based observations. ULF waves of this period have been linked to processes active in the near-Earth magnetotail just prior to the substorm expansion phase (e.g., Rae, Mann, Angelopoulos, et al., 2009; Rae, Mann, Murphy, et al., 2009).

First, we presented results from the THEMIS spacecraft, showing that the ULF waves in the near-Earth magnetotail are likely broadband (within the Pi1–2 range), potentially ruling out more narrow-band instabilities such as the current-driven Alfvénic instability (e.g., Perraut et al., 2000). The exponential wave growth is observed a few minutes prior to ionospheric-defined substorm onset and the observation of fast planetward flows in the magnetotail. The ground stations most closely conjugate with the spacecraft, and close to the onset epicenter, show signatures consistent with those made by the spacecraft. However, there is evidence that the shorter period waves are delayed and have weaker signatures. We also see evidence for auroral beads within the conjugate and brightening auroral arc.

Second, we presented delay maps using a wide array of ground magnetometer stations demonstrating a clear onset epicenter indicative of the localized activation of onset-related processes in the magnetotail. Consistently, the onset of each period band is shown to spread coherently from an epicenter, with the longest periods showing the fastest spread. Onset is observed to spread fastest westward of the epicenter, at up to 90 km for the longest period bands. At shorter periods the spread westward is slower, below 10 km. Latitudinal spread of the onset varies between 5 and 10 km at the longer periods, to ≤5 km at the shorter periods. Onset is also only seen at the shorter periods in a much more limited region around the epicenter, beyond which no significant ULF wave activity of that period is observed. Where present, shorter periods also present with greatly reduced PSD on the ground, relative to the space-based observations. These results could be explained by preferential damping of shorter period waves (c.f., shear Alfvén waves Kalmoni et al., 2018) in the magnetotail. There is also evidence for a second epicenter located at a lower latitudes for longer wave periods, perhaps due to their being two distinct paths minimizing the travel time from the initial disturbance to the ionosphere (e.g., Chi et al., 2009; Rae et al., 2017).

Third, we have inferred the travel times between the spacecraft in the near-Earth magnetotail and the ground. ULF waves with periods below ~50 s are generally consistent with travel times of between 1 and 2 min, while those with greater periods show delays of a minute or less. Once more, this difference could be the result of shorter period waves being more heavily damped, and therefore rising above the defined background level later in the event.

Overall, our study confirms that onset-related ULF waves appear to be generated in a localized region of the near-Earth magnetotail. Our work highlights a series of complex spatiotemporal relationships between tail activations and ULF waves on the ground. Nevertheless, using CWT wavelet techniques, we demonstrate how these relationships can be disentangled. Exploiting the techniques presented here will be key to pin-pointing the causal connections between tail processes and ionospheric signatures of onset. This includes the sequence of events at onset, spanning the generation of auroral beads, establishment of the SCW, and the poleward and westward expansion of the aurora in the WTS.

Data Availability Statement

Data provided by the Geophysical Institute Magnetometer Array operated by the Geophysical Institute, University of Alaska are available online (https://www.gi.alaska.edu/monitors/magnetometer/archive). THEMIS data are available online (http://themis.ssl.berkeley.edu/data/themis/).

References

Akasofu, S.-I. (1964). The development of the auroral substorm. *Planetary and Space Science*, *12*(4), 273–282. https://doi.org/10.1016/0032-0633(64)90151-5

Akasofu, S.-I. (1977). Physics of magnetospheric substorms. Research supported by NSF, NASA, ERDA, and U.S. Air Force. Dordrecht, D. Reidel Publishing Co. (Astrophysics and Space Science Library. Volume 47), 1977. 619 p. 47. https://adsabs.harvard.edu/abs/1977nsf....47.....A

Angelopoulos, V. (2008). The THEMIS mission. *Space Science Reviews*, *141*(1–4), 5–34. https://doi.org/10.1007/s11214-008-9336-1

Angelopoulos, V., Baumjohann, W., Kennel, C. F., Coroniti, F. V., Kivelson, M. G., Pellat, R., et al. (1992). Bursty bulk flows in the inner central plasma sheet. *Journal of Geophysical Research*, *97*(A4), 4027. https://doi.org/10.1029/91JA02701

Angelopoulos, V., Kennel, C. F., Coroniti, F. V., Pellat, R., Kivelson, M. G., Walker, R. J., et al. (1994). Statistical characteristics of bursty bulk flow events. *Journal of Geophysical Research*, *99*(A11), 21257. https://doi.org/10.1029/94JA01263

Angelopoulos, V., McFadden, J. P., Larson, D., Carlson, C. W., Mende, S. B., Frey, H., et al. (2008). Tail reconnection triggering substorm onset. *Science*, *321*(5891), 931–935. https://doi.org/10.1126/science.1160495

Arnoldy, R. L., Rajashekar, R., Cahill, L. J., Engebretson, M. J., Rosenberg, T. J., & Mende, S. B. (1987). Simultaneous measurement of aurora-related, irregular magnetic pulsations at northern and southern high latitudes. *Journal of Geophysical Research*, *92*(A11), 12221. https://doi.org/10.1029/JA092iA11p12221

Atkinson, G. (1967). The current system of geomagnetic bays. *Journal of Geophysical Research*, *72*(23), 6063–6067. https://doi.org/10.1029/JZ072i023p06063

Auster, H. U., Glassmeier, K. H., Magnes, W., Aydogar, O., Baumjohann, W., Constantinescu, D., et al. (2009). The THEMIS fluxgate magnetometer, *The themis mission* (pp. 235–264). New York, NY: Springer New York. https://doi.org/10.1007/978-0-387-89820-9_11

Baker, D. N., Pulkkinen, T. I., Angelopoulos, V., Baumjohann, W., & McPherron, R. L. (1996). Neutral line model of substorms: Past results and present view. *Journal of Geophysical Research*, *101*(A6), 12,975–13,010. https://doi.org/10.1029/95JA03753

Baumjohann, W., Paschmann, G., & Lühr, H. (1990). Characteristics of high-speed ion flows in the plasma sheet. *Journal of Geophysical Research*, *95*(A4), 3801. https://doi.org/10.1029/JA095iA04p03801

Bosinger, T., & Yahnin, A. (1987). Pi1B type magnetic pulsation as a high time resolution monitor of substorm development. *Annales Geophysicae*, *5*, 231–237.

Chang, T.-F., & Cheng, C.-Z. (2015). Relationship between wave-like auroral arcs and Pi2 disturbances in plasma sheet prior to substorm onset. *Earth, Planets and Space*, *67*(1), 168. https://doi.org/10.1186/s40623-015-0334-8

Chaston, C. C., Bonnell, J. W., Clausen, L., & Angelopoulos, V. (2012). Correction to "Energy transport by kinetic-scale electromagnetic waves in fast plasma sheet flows". *Journal of Geophysical Research*, *117*, A12205. https://doi.org/10.1029/2012JA018476

Cheng, C. (2004). Physics of substorm growth phase, onset, and dipolarization. *Space Science Reviews*, *113*(1/2), 207–270. https://doi.org/10.1023/B:SPAC.0000042943.59976.0e

Chi, P. J., Russell, C. T., & Ohtani, S. (2009). Substorm onset timing via traveltime magnetoseismology. *Geophysical Research Letters*, *36*, L08107. https://doi.org/10.1029/2008GL036574

Donovan, E., Liu, W., Liang, J., Spanswick, E., Voronkov, I., Connors, M., et al. (2008). Simultaneous THEMIS in situ and auroral observations of a small substorm. *Geophysical Research Letters*, *35*, L17S18. https://doi.org/10.1029/2008GL033794

Ergun, R. E., Goodrich, K. A., Stawarz, J. E., Andersson, L., & Angelopoulos, V. (2015). Large-amplitude electric fields associated with bursty bulk flow braking in the Earth's plasma sheet. *Journal of Geophysical Research: Space Physics*, *120*, 1832–1844. https://doi.org/10.1002/2014JA020165

Farge, M. (1992). Wavelet transforms and their applications to turbulence. *Annual Review of Fluid Mechanics*, *24*(1), 395–458. https://doi.org/10.1146/annurev.fl.24.010192.002143

Ferdousi, B., & Raeder, J. (2016). Signal propagation time from the magnetotail to the ionosphere: OpenGGCM simulation. *Journal of Geophysical Research: Space Physics*, *121*, 6549–6561. https://doi.org/10.1002/2016JA022445

Forsyth, C., Rae, I. J., Coxon, J. C., Freeman, M. P., Jackman, C. M., Gjerloev, J., & Fazakerley, A. N. (2015). A new technique for determining Substorm Onsets and Phases from Indices of the Electrojet (SOPHIE). *Journal of Geophysical Research: Space Physics*, *120*, 10,592–10,606. https://doi.org/10.1002/2015JA021343

Gjerloev, J. W. (2012). The SuperMAG data processing technique. *Journal of Geophysical Research*, *117*, A09213. https://doi.org/10.1029/2012JA017683

Henderson, M. G. (1994). Implications of Viking Imager results for substorm models (Thesis (PH.D.). *Source: Dissertation Abstracts International* (Volume 56–01, Section B, p. 0289). Canada, University of Calgary. https://adsabs.harvard.edu/abs/1994PhDT........53H

Hones, E. W. (1976). The magnetotail - Its generation and dissipation. *Physics of Solar Planetary Environments*, *2*, 558–571.

Hones, E. W., Baker, D. N., Bame, S. J., Feldman, W. C., Gosling, J. T., McComas, D. J., et al. (1984). Structure of the magnetotail at 220 R_E and its response to geomagnetic activity. *Geophysical Research Letters*, *11*(1), 5–7. https://doi.org/10.1029/GL011i001p00005

Hunter, J. D. (2007). Matplotlib: A 2D graphics environment. *Computing in Science & Engineering*, *9*(3), 90–95. https://doi.org/10.1109/MCSE.2007.55

Imber, S. M., Slavin, J. A., Auster, H. U., & Angelopoulos, V. (2011). A THEMIS survey of flux ropes and traveling compression regions: Location of the near-Earth reconnection site during solar minimum. *Journal of Geophysical Research*, *116*, A02201. https://doi.org/10.1029/2010JA016026

Jacobs, J. A., Kato, Y., Matsushita, S., & Troitskaya, V. A. (1964). Classification of geomagnetic micropulsations. *Geophysical Journal of the Royal Astronomical Society*, *8*(3), 341–342. https://doi.org/10.1111/j.1365-246X.1964.tb06301.x

Kaiser, G., & Hudgins, L. H. (1995). *A friendly guide to wavelets* (Vol. 48). New York: Birkhäuser. https://doi.org/10.1063/1.2808105

Kalmoni, N. M. E., Rae, I. J., Murphy, K. R., Forsyth, C., Watt, C. E., & Owen, C. J. (2017). Statistical azimuthal structuring of the substorm onset arc: Implications for the onset mechanism. *Geophysical Research Letters*, *44*, 2078–2087. https://doi.org/10.1002/2016GL071826

Kalmoni, N. M. E., Rae, I. J., Watt, C. E. J., Murphy, K. R., Forsyth, C., & Owen, C. J. (2015). Statistical characterization of the growth and spatial scales of the substorm onset arc. *Journal of Geophysical Research: Space Physics*, *120*, 8503–8516. https://doi.org/10.1002/2015JA021470

Kalmoni, N. M. E., Rae, I. J., Watt, C. E. J., Murphy, K. R., Samara, M., Michell, R. G., et al. (2018). A diagnosis of the plasma waves responsible for the explosive energy release of substorm onset. *Nature Communications*, *9*(1), 4806. https://doi.org/10.1038/s41467-018-07086-0

Keiling, A. (2012). Pi2 pulsations driven by ballooning instability. *Journal of Geophysical Research*, *117*, A03228. https://doi.org/10.1029/2011JA017223

Keiling, A., Fujimoto, M., Hasegawa, H., Honary, F., Sergeev, V., Semenov, V. S., et al. (2006). Association of Pi2 pulsations and pulsed reconnection: Ground and cluster observations in the tail lobe at 16$_E$. *Annales Geophysicae*, *24*(12), 3433–3449. https://doi.org/10.5194/angeo-24-3433-2006

Kepko, L., & Kivelson, M. (1999). Generation of Pi2 pulsations by bursty bulk flows. *Journal of Geophysical Research*, *104*(A11), 25,021–25,034. https://doi.org/10.1029/1999JA900361

Kepko, L., McPherron, R. L., Amm, O., Apatenkov, S., Baumjohann, W., Birn, J., et al. (2015). Substorm current wedge revisited. *Space Science Reviews*, *190*(1–4), 1–46. https://doi.org/10.1007/s11214-014-0124-9

Kepko, L., Spanswick, E., Angelopoulos, V., Donovan, E., McFadden, J., Glassmeier, K.-H., et al. (2009). Equatorward moving auroral signatures of a flow burst observed prior to auroral onset. *Geophysical Research Letters*, *36*, L24104. https://doi.org/10.1029/2009GL041476

Lester, M., Hughes, J. W., & Singer, H. J. (1983). Polarization patterns of Pi2 magnetic pulsations and the substorm current wedge. *Journal of Geophysical Research*, *88*(A10), 7958. https://doi.org/10.1029/JA088iA10p07958

Liu, Y., Liang, X. S., & Weisberg, R. H. (2007). Rectification of the Bias in the Wavelet Power Spectrum. https://doi.org/10.1175/2007JTECHO511.1

Lui, A. T. Y. (1996). Current disruption in the Earth's magnetosphere: Observations and models. *Journal of Geophysical Research*, *101*(A6), 13,067–13,088. https://doi.org/10.1029/96JA00079

Lui, A. (2004). Potential plasma instabilities for substorm expansion onsets. *Space Science Reviews*, *113*(1/2), 127–206. https://doi.org/10.1023/B:SPAC.0000042942.00362.4e

Lui, A. T. Y., Chang, C.-L., Mankofsky, A., Wong, H.-K., & Winske, D. (1991). A cross-field current instability for substorm expansions. *Journal of Geophysical Research*, *96*(A7), 11389. https://doi.org/10.1029/91JA00892

Lui, A. T. Y., Volwerk, M., Dunlop, M. W., Alexeev, I. V., Fazakerley, A. N., Walsh, A. P., et al. (2008). Near-Earth substorm features from multiple satellite observations. *Journal of Geophysical Research*, *113*, A07S26. https://doi.org/10.1029/2007JA012738

Lysak, R. L., & Lotko, W. (1996). On the kinetic dispersion relation for shear Alfvén waves. *Journal of Geophysical Research*, *101*(A3), 5085–5094. https://doi.org/10.1029/95JA03712

Mann, I. R., Milling, D. K., Rae, I. J., Ozeke, L. G., Kale, A., Kale, Z. C., et al. (2008). The upgraded CARISMA magnetometer array in the THEMIS era. *Space Science Reviews*, *141*(1–4), 413–451. https://doi.org/10.1007/s11214-008-9457-6

McFadden, J. P., Carlson, C. W., Larson, D., Ludlam, M., Abiad, R., Elliott, B., et al. (2009). The THEMIS ESA plasma instrument and in-flight calibration. In *The themis mission* (pp. 277–302). New York, NY: Springer New York. https://doi.org/10.1007/978-0-387-89820-9_13

McKinney, W. (2010). Data structures for statistical computing in Python. https://conference.scipy.org/proceedings/scipy2010/mckinney.html

McPherron, R. L. (1970). Growth phase of magnetospheric substorms (Tech. Rep. No. 28). https://citeseerx.ist.psu.edu/viewdoc/download?doi=10.1.1.452.9720&rep=rep1&type=pdf

McPherron, R. L., Russell, C. T., & Aubry, M. P. (1973). Satellite studies of magnetospheric substorms on August 15, 1968: 9. Phenomenological model for substorms. *Journal of Geophysical Research*, *78*(16), 3131–3149. https://doi.org/10.1029/JA078i016p03131

Meyer, Y. (1990). *Ondelettes et Opérateurs*. Paris: Hermann. Retrieved from https://books.google.co.uk/books/about/Ondelettes_et_operateurs.html?id=2vtBuwEACAAJ&redir_esc=y

Milling, D. K., Rae, I. J., Mann, I. R., Murphy, K. R., Kale, A., Russell, C. T., et al. (2008). Ionospheric localisation and expansion of long-period Pi1 pulsations at substorm onset. *Geophysical Research Letters*, *35*, L17S20. https://doi.org/10.1029/2008GL033672

Morlet, J., Arens, G., Fourgeau, E., & Giard, D. (1982). Wave propagation and sampling theory—Part I. Complex signal and scattering in multilayered media. *Geophysics*, *47*(2), 203–221. https://doi.org/10.1190/1.1441328

Motoba, T., Hosokawa, K., Kadokura, A., & Sato, N. (2012). Magnetic conjugacy of northern and southern auroral beads. *Geophysical Research Letters*, *39*, L08108. https://doi.org/10.1029/2012GL051599

Motoba, T., Ohtani, S., Donovan, E. F., & Angelopoulos, V. (2015). On a possible connection between the longitudinally propagating near-Earth plasma sheet and auroral arc waves: A reexamination. *Journal of Geophysical Research: Space Physics*, *120*, 432–444. https://doi.org/10.1002/2014JA020694

Murphy, K. R., Jonathan Rae, I., Mann, I. R., Milling, D. K., Watt, C. E., Ozeke, L., et al. (2009). Wavelet-based ULF wave diagnosis of substorm expansion phase onset. *Journal of Geophysical Research*, *114*, A00C16. https://doi.org/10.1029/2008JA013548

Murphy, K. R., Mann, I. R., Rae, I. J., Walsh, A. P., & Frey, H. U. (2014). Inner magnetospheric onset preceding reconnection and tail dynamics during substorms: Can substorms initiate in two different regions? *Journal of Geophysical Research: Space Physics*, *119*, 9684–9701. https://doi.org/10.1002/2014JA019795

Murphy, K. R., Rae, I. J., Mann, I. R., & Milling, D. K. (2011). On the nature of ULF wave power during nightside auroral activations and substorms: 1. Spatial distribution. *Journal of Geophysical Research*, *116*, A00I21. https://doi.org/10.1029/2010JA015757

Murphy, K. R., Rae, I. J., Mann, I. R., Walsh, A. P., Milling, D. K., & Kale, A. (2011). The dependence of Pi2 waveforms on periodic velocity enhancements within bursty bulk flows. *Annales Geophysicae*, *29*(3), 493–509. https://doi.org/10.5194/angeo-29-493-2011

Nagai, T., Mukai, T., Yamamoto, T., Nishida, A., Kokubun, S., & Lepping, R. P. (1997). Plasma sheet pressure changes during the substorm growth phase. *Geophysical Research Letters*, *24*(8), 963–966. https://doi.org/10.1029/97GL00374

Newell, P. T., & Gjerloev, J. W. (2011). Evaluation of SuperMAG auroral electrojet indices as indicators of substorms and auroral power. *Journal of Geophysical Research*, *116*, A12211. https://doi.org/10.1029/2011JA016779

Nishimura, Y., Lyons, L., Zou, S., Angelopoulos, V., & Mende, S. (2010). Substorm triggering by new plasma intrusion: THEMIS all-sky imager observations. *Journal of Geophysical Research*, *115*, A07222. https://doi.org/10.1029/2009JA015166

Nosé, M., Iyemori, T., Takeda, M., Kamei, T., Milling, D. K., Orr, D., et al. (1998). Automated detection of Pi2 pulsations using wavelet analysis: 1. Method and an application for substorm monitoring. *Earth, Planets and Space*, *50*(9), 773–783. https://doi.org/10.1186/BF03352169

Ohtani, S.-I. (2004). Flow bursts in the plasma sheet and auroral substorm onset: Observational constraints on connection between midtail and near-earth substorm processes. *Space Science Reviews*, *113*(1/2), 77–96. https://doi.org/10.1023/B:SPAC.0000042940.59358.2f

Olson, J. V. (1999). Pi2 pulsations and substorm onsets: A review. *Journal of Geophysical Research*, *104*, 17,499–17,520. https://doi.org/10.1029/1999JA900086

Panov, E. V., Sergeev, V. A., Pritchett, P. L., Coroniti, F. V., Nakamura, R., Baumjohann, W., et al. (2012). Observations of kinetic ballooning/interchange instability signatures in the magnetotail. *Geophysical Research Letters*, *39*, L08110. https://doi.org/10.1029/2012GL051668

Pedregosa, F., Varoquaux, G., Gramfort, A., Michel, V., Thirion, B., Grisel, O., et al. (2011). Scikit-learn: Machine learning in Python. *Journal of Machine Learning Research*, *12*, 2825–2830. https://jmlr.org/papers/v12/pedregosa11a.html

Perraut, S., Le Contel, O., Roux, A., & Pedersen, A. (2000). Current-driven electromagnetic ion cyclotron instability at substorm onset. *Journal of Geophysical Research*, *105*(A9), 21,097–21,107. https://doi.org/10.1029/2000JA900059

Rae, I. J., Mann, I. R., Angelopoulos, V., Murphy, K. R., Milling, D. K., Kale, A., et al. (2009). Near-Earth initiation of a terrestrial substorm. *Journal of Geophysical Research*, *114*, A07220. https://doi.org/10.1029/2008JA013771

Rae, I. J., Mann, J. R., Murphy, I. R., Milling, K. R., Parent, D. K., Angelopoulos, A., et al. (2009). Timing and localization of ionospheric signatures associated with substorm expansion phase onset timing and localization of ionospheric signatures associated with substorm expansion phase onset Timing and localization of ionospheric signatures associated. *Journal of Geophysical Research*, *114*, A00C09. https://doi.org/10.1029/2008JA013559

Rae, I. J., Murphy, K. R., Watt, C. E. J., & Mann, I. R. (2011). On the nature of ULF wave power during nightside auroral activations and substorms: 2. Temporal evolution. *Journal of Geophysical Research*, *116*, A00I22. https://doi.org/10.1029/2010JA015762

Rae, I. J., Murphy, K. R., Watt, C. E. J., Mann, I. R., Yao, Z., Kalmoni, N. M. E., et al. (2017). Using ultra-low frequency waves and their characteristics to diagnose key physics of substorm onset. *Geoscience Letters*, *4*(1), 23. https://doi.org/10.1186/s40562-017-0089-0

Rae, I. J., & Watt, C. E. (2016). ULF waves above the nightside auroral oval during substorm onset. In *Low-frequency waves in space plasmas* (pp. 99–120). Hoboken, NJ: American Geophysical Union (AGU). https://doi.org/10.1002/9781119055006.ch7

Rae, I. J., Watt, C. E. J., Mann, I. R., Murphy, K. R., Samson, J. C., Kabin, K., & Angelopoulos, V. (2010). Optical characterization of the growth and spatial structure of a substorm onset arc. *Journal of Geophysical Research*, *115*, A10222. https://doi.org/10.1029/2010JA015376

Rae, I. J., Watt, C. E. J., Murphy, K. R., Frey, H. U., Ozeke, L. G., Milling, D. K., & Mann, I. R. (2012). The correlation of ULF waves and auroral intensity before, during and after substorm expansion phase onset. *Journal of Geophysical Research*, *117*, A08213. https://doi.org/10.1029/2012JA017534

Roux, A., Perraut, S., Robert, P., Morane, A., Pedersen, A., Korth, A., et al. (1991). Plasma sheet instability related to the westward traveling surge. *Journal of Geophysical Research*, *96*(A10), 17697. https://doi.org/10.1029/91JA01106

Russell, C. T., Jackman, C. M., Wei, H. Y., Bertucci, C., & Dougherty, M. K. (2008). Titan's influence on Saturnian substorm occurrence. *Geophysical Research Letters*, *35*, L12105. https://doi.org/10.1029/2008GL034080

Saito, M. H., Miyashita, Y., Fujimoto, M., Shinohara, I., Saito, Y., & Mukai, T. (2008). Modes and characteristics of low-frequency MHD waves in the near-Earth magnetotail prior to dipolarization: Fitting method. *Journal of Geophysical Research*, *113*, A06201. https://doi.org/10.1029/2007JA012778

Sergeev, V. A., Dmitrieva, N. P., Stepanov, N. A., Sormakov, D. A., Angelopoulos, V., & Runov, A. V. (2015). On the plasma sheet dependence on solar wind and substorms and its role in magnetosphere-ionosphere coupling. *Earth, Planets and Space*, *67*(1), 133. https://doi.org/10.1186/s40623-015-0296-x

Shiokawa, K., Baumjohann, W., & Haerendel, G. (1997). Braking of high-speed flows in the near-Earth tail. *Geophysical Research Letters*, *24*(10), 1179–1182. https://doi.org/10.1029/97GL01062

Shiokawa, K., Baumjohann, W., Haerendel, G., Paschmann, G., Fennell, J. F., Friis-Christensen, E., et al. (1998). High-speed ion flow, substorm current wedge, and multiple Pi2 pulsations. *Journal of Geophysical Research*, *103*(A3), 4491–4507. https://doi.org/10.1029/97JA01680

Slavin, J. A., Baker, D. N., Craven, J. D., Elphic, R. C., Fairfield, D. H., Frank, L. A., et al. (1989). CDAW 8 observations of plasmoid signatures in the geomagnetic tail: An assessment. *Journal of Geophysical Research*, *94*(A11), 15153. https://doi.org/10.1029/JA094iA11p15153

Slavin, J. A., Owen, C. J., Kuznetsova, M. M., & Hesse, M. (1995). ISEE 3 observations of plasmoids with flux rope magnectic topologies. *Geophysical Research Letters*, *22*, 2061–2064. https://doi.org/10.1029/95GL01977

Smith, A. W., Rae, I. J., Forsyth, C., Watt, C. E. J., & Murphy, K. R. (2020). On the magnetospheric ULF wave counterpart of substorm onset. *Journal of Geophysical Research: Space Physics*, *125*, e2019JA027573. https://doi.org/10.1029/2019JA027573

Tamao, T. (1964). The structure of three-dimensional hydromagnetic waves in a uniform cold plasma. *Journal of Geomagnetism and Geoelectricity*, *16*(2), 89–114. https://doi.org/10.5636/jgg.16.89

Torrence, C., Compo, G. P., Torrence, C., & Compo, G. P. (1998). A practical guide to wavelet analysis. *Bulletin of the American Meteorological Society*, *79*(1), 61–78. https://doi.org/10.1175/1520-0477(1998)079<0061:APGTWA>2.0.CO;2

Tsyganenko, N. A. (1989). A magnetospheric magnetic field model with a warped tail current sheet. *Planetary and Space Science*, *37*(1), 5–20. https://doi.org/10.1016/0032-0633(89)90066-4

Tsyganenko, N. A., & Sitnov, M. I. (2005). Modeling the dynamics of the inner magnetosphere during strong geomagnetic storms. *Journal of Geophysical Research*, *110*, A03208. https://doi.org/10.1029/2004JA010798

Uozumi, T., Yoshikawa, A., & Ohtani, S. (2020). Formation of a 3-D oscillatory current system associated with global high-correlation PI 2 event: A case study. *Journal of Geophysical Research: Space Physics*, *125*, e2019JA026988. https://doi.org/10.1029/2019JA026988

Uritsky, V. M., Liang, J., Donovan, E., Spanswick, E., Knudsen, D., Liu, W., et al. (2009). Longitudinally propagating arc wave in the pre-onset optical aurora. *Geophysical Research Letters*, *36*, L21103. https://doi.org/10.1029/2009GL040777

van der Walt, S., Colbert, S. C., & Varoquaux, G. (2011). The NumPy array: A structure for efficient numerical computation. *Computing in Science & Engineering*, *13*(2), 22–30. https://doi.org/10.1109/MCSE.2011.37

Virtanen, P., Gommers, R., Oliphant, T. E., Haberland, M., Reddy, T., Cournapeau, D., et al. (2020). SciPy 1.0: Fundamental algorithms for scientific computing in Python. *Nature Methods*, *17*, 261–272. https://doi.org/10.1038/s41592-019-0686-2

Voronkov, I., Rankin, R., Frycz, P., Tikhonchuk, V. T., & Samson, J. C. (1997). Coupling of shear flow and pressure gradient instabilities. *Journal of Geophysical Research*, *102*(A5), 9639–9650. https://doi.org/10.1029/97JA00386

Walsh, A. P., Rae, I. J., Fazakerley, A. N., Murphy, K. R., Mann, I. R., Watt, C. E. J., et al. (2010). Comprehensive ground-based and in situ observations of substorm expansion phase onset. *Journal of Geophysical Research*, *115*, A00I13. https://doi.org/10.1029/2010JA015748

Watt, C. E. J., & Rankin, R. (2007). Electron acceleration due to inertial Alfvén waves in a non-Maxwellian plasma. *Journal of Geophysical Research*, *112*, A04214. https://doi.org/10.1029/2006JA011907

Wing, S., Gkioulidou, M., Johnson, J. R., Newell, P. T., & Wang, C.-P. (2013). Auroral particle precipitation characterized by the substorm cycle. *Journal of Geophysical Research: Space Physics*, *118*, 1022–1039. https://doi.org/10.1002/jgra.50160